materials

MDPI

Article

Mesoscale Modeling of Thermal Conduction in Asphalt Mixtures Considering Aggregate Morphology, Gradation, and Air-Void Content, Verified by Dual Numerical Solvers

Songhao Han [1], Jiawei Zhang [2] and Dongdong Yuan [1,*]

[1] School of Highway, Chang'an University, Xi'an 710064, China; 2024902207@chd.edu.cn
[2] Chang'an Dublin International College, Chang'an University, Xi'an 710064, China
* Correspondence: ddy@chd.edu.cn

Abstract

The effective thermal conductivity k_{eff} of asphalt mixtures is a key input for pavement thermal analysis, governing rutting and cracking predictions. Current prediction methods have limitations: layered homogeneous models cannot resolve the mesoscale heat-conduction mechanisms, while mesoscale models often idealize aggregate shapes, treat voids incompletely, and lack verified numerical reliability. This study develops a unified, parametric three-phase mesoscale framework in which aggregate morphology, gradation, and air-void content are controlled independently. Steady-state heat conduction is solved by two independent methods: a Python 3.12.6 finite-volume (FVM) solver and finite-element (FEM) simulations in COMSOL 6.3. Across 14 cases, the two approaches differ by 2.1–4.7% (mean 3.0%), and both reproduce the analytical solution of the layered benchmark within 0.01%. Within the 3–6% design air-void range, the simulated k_{eff} is 1.47–1.61 W/(m·K) over the studied composition space, consistent with measured data. It decreases approximately linearly with air-void content, by 0.024 W/(m·K) per percentage point (FVM); a Maxwell–Eucken expression reproduces 89% of this reduction. Aggregate morphology affects conductivity mainly through packing. A generalized Maxwell–Eucken expression matches all numerical results to within 3.0%, a practical prediction tool; phase properties are fixed for a single aggregate mineralogy, a key limitation.

Keywords: asphalt mixture; thermal properties; finite volume method; finite element method; representative volume element; effective medium theory; voxel model; numerical verification

Check for updates

Academic Editor: Jorge Carvalho Pais

Received: 29 October 2026
Revised: 18 November 2026
Accepted: 23 November 2026
Published: 25 November 2026

Copyright: © 2026 by the authors. Licensee MDPI, Basel, Switzerland. This article is an open access article distributed under the terms and conditions of the Creative Commons Attribution (CC BY) license.

1. Introduction

Pavement temperature fields are a major driver of rutting, low-temperature cracking, and blistering. They also determine the contribution of asphalt surfaces to the urban heat island effect and to heat-harvesting and snow-melting systems [1–3]. In all these applications, the effective thermal conductivity k_{eff} of the mixture is a key input parameter.

In standard engineering practice, each pavement layer is treated as a homogeneous slab with a single effective conductivity [1,2]. Such layered models, however, cannot capture the measurable conductivity differences among mixtures with the same nominal composition but different compaction states and void distributions [1,3]. Nor do they provide a mechanistic link between the microstructure and the effective property. This restricts their use in designing pavements whose thermal performance is deliberately engineered through the mesostructure.

Mesoscale modeling overcomes this limitation by explicitly resolving the aggregate and void phases. Recent studies have taken several approaches: hierarchical multiscale finite-element models of three-phase microstructures [4–6], Voronoi-based random aggregate models with controlled sphericity and orientation [7], and microstructures reconstructed from X-ray computed tomography (CT) [8,9].

Most published studies are three-dimensional, whereas two-dimensional simplifications are generally limited to exploratory parameter screening; particle-based and discrete-element treatments remain comparatively rare for heat conduction. Existing mesoscale studies also differ widely in their validation practice: several report only internal consistency checks, and their computational cost is rarely stated, which hinders direct comparison of accuracy per unit cost. Alongside numerical models, effective-medium theories provide closed-form estimates of the effective conductivity from the phase volume fractions: the Maxwell and Maxwell–Garnett forms [10,11], the Hashin–Shtrikman bounds [12], the Bruggeman self-consistent scheme [13], and the Lewis–Nielsen model [14], with the series and parallel arrangements as limiting cases. These models are computationally trivial but were developed for idealized microstructures (dilute inclusions or self-similar media), so their accuracy for realistic three-phase asphalt microstructures must be established by systematic comparison against resolved mesoscale simulations—the approach adopted in Section 5.3.

Three critical knowledge gaps persist in the mesoscale modeling of thermal conduction in asphalt mixtures. First, the investigation of the parameter space remains fragmented: individual studies typically vary a limited subset of the controlling factors (e.g., gradation, air-void content, and aggregate morphology) while holding the others constant. Consequently, their findings cannot be synthesized into a unified framework. Any explicit mesoscale resolution must clearly exceed this baseline, given that simple cubic-cell models have been argued to achieve comparable accuracy [15].

Second, aggregate shapes are either highly idealized (e.g., spheres or ellipsoids [16]) or reconstructed from CT scans, which is cost-prohibitive and limited by sample sizes. Although the most closely related prior work generates random polyhedral aggregates, it neither addresses the morphology–packing–conduction coupling nor reports the reliability of its numerical workflow [17]. Moreover, most 3D mesoscale studies rely on cross-software integration or CT reconstruction [8,9,16,17], necessitating multiple commercial licenses and cumbersome manual data transfer. In contrast, the present framework generates the complete three-phase geometry within a single Python pipeline and solves the thermal problem via two independent numerical routes.

Third, the numerical reliability of existing results—such as solver cross-validation, voxel-resolution convergence, and Representative Volume Element (RVE) statistical representativeness—is rarely demonstrated [5,17]. Consequently, analytical models linking microstructural phase fractions to the macroscopic effective conductivity [18] have rarely been validated against systematically resolved three-phase mesoscale simulations for engineering prediction.

This study addresses these gaps through three contributions. First, a unified parametric modeling framework is developed in which aggregate morphology (controlled by a perturbation coefficient), gradation, and air-void content can be varied independently within a single algorithmic pipeline. Second, all Boolean operations are performed on the generation side using a robust geometry engine, and the thermal problem is solved by two independent numerical routes; their agreement, together with an analytical benchmark, establishes the numerical reliability of the results. Third, the computed k_{eff} values are systematically compared with a generalized Maxwell–Eucken analytical model [10,11] and with experimental data from the literature, thereby quantifying the physical mechanisms by

which voids and aggregate morphology govern heat conduction. This comparative analysis covers the practical design range of air-void contents, and the analytical model is used to decompose the individual phase contributions, demonstrating its validity as a practical engineering prediction tool.

The objective of this study is to establish a unified, numerically verified, three-phase mesoscale framework that quantifies how aggregate morphology, gradation, and air-void content jointly govern the effective thermal conductivity, and to validate an analytical model suitable for engineering prediction. Three hypotheses are tested: (H1) the effective conductivity decreases approximately linearly with air-void content over the 3–6% design range, without saturation; (H2) aggregate morphology acts on conduction chiefly through packing efficiency rather than through interface tortuosity at fixed composition; and (H3) a generalized Maxwell–Eucken expression reproduces the simulated conductivity within 3% across the studied composition space.

2. Materials and Methods

2.1. Model Framework and Material Phases

The mixture is represented by a three-phase representative volume element (RVE): aggregate, asphalt mortar, and air void. The mortar phase consists of a fine aggregate matrix (FAM) formed by homogenizing the asphalt mastic (binder–filler blend) with fine aggregates smaller than 2.36 mm, consistent with established mesoscale modeling practice [4,7,19]: homogenizing the asphalt mastic ($k \approx 0.75$ W/(m·K)—the asphalt-phase value adopted in the mesoscale homogenization practice [4], compiled therein from standard heat-transfer references—with the fine aggregate fraction (about 35% by volume of the mortar, $k = 2.8$ W/(m·K)) through a Maxwell-type two-phase expression yields W/(m·K), the value adopted in Table 1 This value exceeds some neat-binder measurements (≈0.2 W/(m·K)); we follow the asphalt-phase value of the mesoscale homogenization practice [4] to remain comparable with [4,7,19], and because measured phase conductivities depend strongly on the measurement technique, the influence of this choice on the results is quantified by the ±33% mortar-conductivity sweep reported in Section 4.6.

Table 1. Phase thermal properties.

Phase	k (W/(m·K))	ρ (kg/m^3)	c_p (J/(kg·K))
Aggregate	2.8	2700	850
Asphalt mortar	1.2	2200	1200
Air void	0.026	1.2	1005

The RVE size must balance statistical representativeness against voxelization cost: an edge length that is too small contains too few particles and suffers from pronounced boundary effects, whereas one that is too large increases the number of elements in the 0.5 mm voxel grid cubically. Accordingly, 50 mm is adopted for AC-13 (100^3 voxels, approximately one million elements) and 70 mm for AC-16/AC-20 (140^3 voxels). The selected edge lengths are approximately 3.5–4.4 times the nominal maximum aggregate size, consistent with the scales commonly used in mesoscale simulations. k_{eff} changes by only 1.1% when the RVE size varies between 40 and 60 mm, and the half-range fluctuation across three independent placements at 50 mm is less than 0.2%; both variations are far smaller than the parametric effects reported in Section 4, indicating that the selected size is already representative.

All particles are placed strictly inside the RVE, with a 0.6 mm mortar shell retained at the boundaries. A minimum surface gap of 0.1–0.2 mm between particles is enforced through exact minimum-distance queries provided by a native geometry engine (manifold3d 3.5.3),

thereby ensuring a continuous, meshable mortar phase without tolerance-based Boolean repairs. Before any result is accepted, a post-placement audit re-checks all particle pairs and the volume conservation of the phase union.

2.2. Aggregate and Void Generation

Aggregate particles are generated using a spherical-coordinate perturbation method. Twenty-six control points are arranged on a sphere: one at each pole and eight azimuthal positions at each of three polar-angle levels ($\theta = 45°$, 90°, and 135°). The radial and angular coordinates of each control point are perturbed independently:

$$r = r_0(1 + \xi), \quad \xi \sim U(-\alpha, \alpha) \tag{1}$$

$$\theta' = \theta + \eta, \quad \varphi' = \varphi + \eta, \quad \eta \sim U(-20°, 20°) \tag{2}$$

where α is the morphology perturbation coefficient. The convex hull of the perturbed points forms a closed polyhedron with irregular angular facets; the hull is then subjected to a uniformly random rotation about its centroid. The coefficient α controls the surface irregularity: the mean sphericity of the generated particles, defined as $\Psi = \pi^{1/3}(6V)^{2/3}/A$, decreases monotonically from 0.944 at $\alpha = 0.1$ to 0.857 at $\alpha = 0.8$ (Figure 1), providing a standard shape descriptor for comparison with natural aggregates. Each particle is validated upon generation to ensure watertightness, positive volume, and the absence of degenerate faces. Air voids are generated by the same method using a larger perturbation coefficient ($\alpha = 0.5$) and a diameter range of 1.0–2.5 mm (diameters uniformly distributed within this window; 3763 voids in the base case), consistent with the void sizes reported for dense-graded mixtures [3,20].

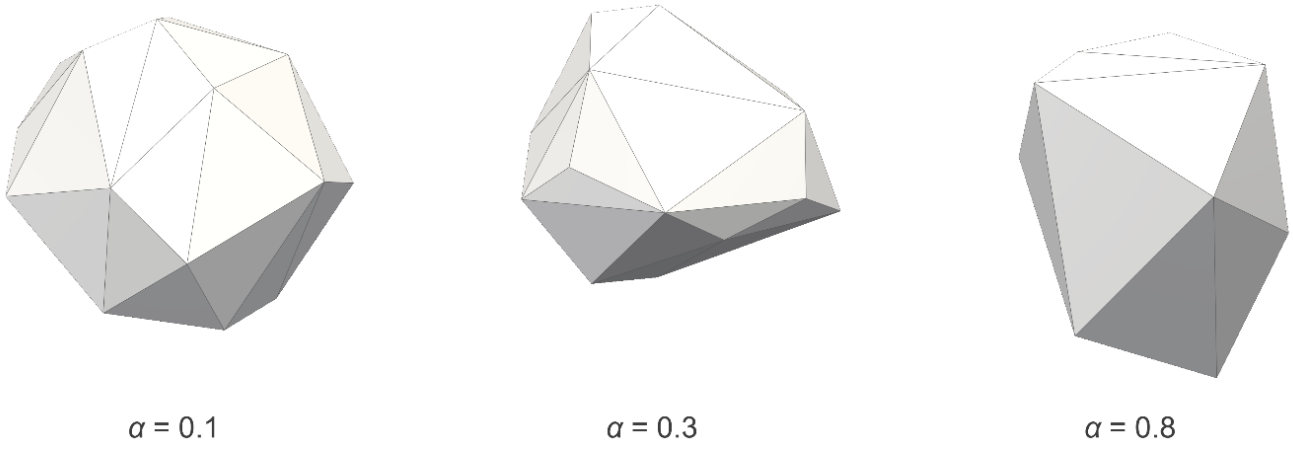


Figure 1. Aggregate particles generated by the spherical-coordinate perturbation method for perturbation coefficients $\alpha = 0.1$, 0.3, and 0.8 (**left** to **right**).

2.3. Model Parameters and Simulation Cases

Particles are packed sequentially from the largest to the smallest size class. Each candidate undergoes a vectorized bounding-sphere and bounding-box rejection test, followed by an exact minimum-distance query (Manifold3D) against all surviving particles; a placement is accepted only when the exact query confirms the required gap. Each size class is allocated a budget of 150,000 placement attempts. Classes that stagnate relax the required gap from 0.2 to 0.1 mm, and high-density aggregate classes that stall at the minimum gap switch to a shuffled 0.5–0.6 mm grid of candidate positions, thereby sampling the remaining free space more completely at the same budget. Void placement additionally uses a distance-field-guided strategy: candidates are sampled from free voxels that can accommodate the

current particle, based on the distance to aggregate surfaces (via KD-tree query) and RVE faces. Oversized voids are redrawn from the lower half of the size window, reflecting the physical tendency of voids to form where space permits; the guidance is heuristic and does not claim to maximize void volume for a given budget. Voids may touch aggregates (as in real compacted mixtures) but never overlap them.

A post-placement audit is mandatory before any result is used: every particle pair is re-verified by exact distance queries, and the manifold union of each phase is compared against the sum of the particle volumes (0.1% tolerance). This check once caught and rejected two defective placements in which aggregate pairs were exactly touching. Because the audit is embedded in the pipeline, any algorithmic regression triggers an explicit error rather than silently contaminating subsequent results.

Table 2 lists the 14 simulation cases. The gradation targets follow the JTG F40-2004 specification [21]: for AC-13, the design volume fractions of the 13.2–16.0, 9.5–13.2, 4.75–9.5, and 2.36–4.75 mm classes are 3.1%, 19.6%, 19.8%, and 13.2%, respectively; the corresponding classes for AC-16 and AC-20 are defined similarly. Particles finer than 2.36 mm are not modeled explicitly. Three series are defined: the void-content series with design air-void contents of 3–8% for AC-13 at $\alpha = 0.2$; the morphology series with $\alpha = 0.1$–0.8 for AC-13 at a 4% design air-void content; and the gradation series with AC-13, AC-16, and AC-20 at $\alpha = 0.2$ and a 4% design air-void content. The achieved phase volume fractions are reported for every case, as the stochastic packing algorithm yields realizable values that may differ from the design targets; all analyses in Section 4 use the achieved values. The void-content series spans 3.0–6.1% in 0.5 percentage-point increments and covers the 3–6% design air-void range of dense-graded mixtures (the 4% Superpave design target of the American Association of State Highway and Transportation Officials (AASHTO) M 323 [22–24] and the EN 13108-1 void-content classes [25]), with 6.12% the maximum achievable void content under the adopted placement constraints.

Table 2. Simulation matrix: design parameters, achieved phase volume fractions, and analysis roles.

Series	Gradation	α	Design Air-Void (%)	Achieved $V_{f,agg}$ (%)	Achieved $V_{f,void}$ (%)	Analysis Role
Void	AC-13	0.2	3.0	35.95	3.00	Air-void parametric series
Void	AC-13	0.2	3.5	35.95	3.50	Air-void parametric series
Void	AC-13	0.2	4.0	35.95	4.00	Base case; resolution, seed, RVE-size, and sensitivity studies
Void	AC-13	0.2	4.5	35.95	4.50	Air-void parametric series
Void	AC-13	0.2	5.0	35.95	5.00	Air-void parametric series
Void	AC-13	0.2	5.5	35.95	5.50	Air-void parametric series
Void	AC-13	0.2	6.0	35.95	6.00	Air-void parametric series
Void	AC-13	0.2	8.0	35.95	6.12	Air-void parametric series
Morphology	AC-13	0.1	4.0	37.91	4.00	Morphology parametric series
Morphology	AC-13	0.3	4.0	34.33	4.00	Morphology parametric series
Morphology	AC-13	0.5	4.0	33.26	4.00	Morphology parametric series
Morphology	AC-13	0.8	4.0	30.71	4.00	Morphology parametric series
Gradation	AC-16	0.2	4.0	39.51	4.00	Cross-validation only (1.0 mm voxels)
Gradation	AC-20	0.2	4.0	41.07	4.00	Cross-validation only (1.0 mm voxels)

Note: α denotes the aggregate morphology perturbation coefficient. Achieved values may differ from the design targets (Section 2.3). All 14 cases enter the FVM–FEM cross-validation (Table 3); the AC-16 and AC-20 cases use 1.0 mm voxels and serve for solver cross-validation only, and their 0.5 mm FVM results enter the gradation analysis (Section 4.4).

Having described the individual modeling steps, we now summarize the overall procedure in Figure 2. The workflow proceeds from gradation input to effective-conductivity extraction through particle generation, packing, auditing, voxelization, and dual FVM/FEM solution.

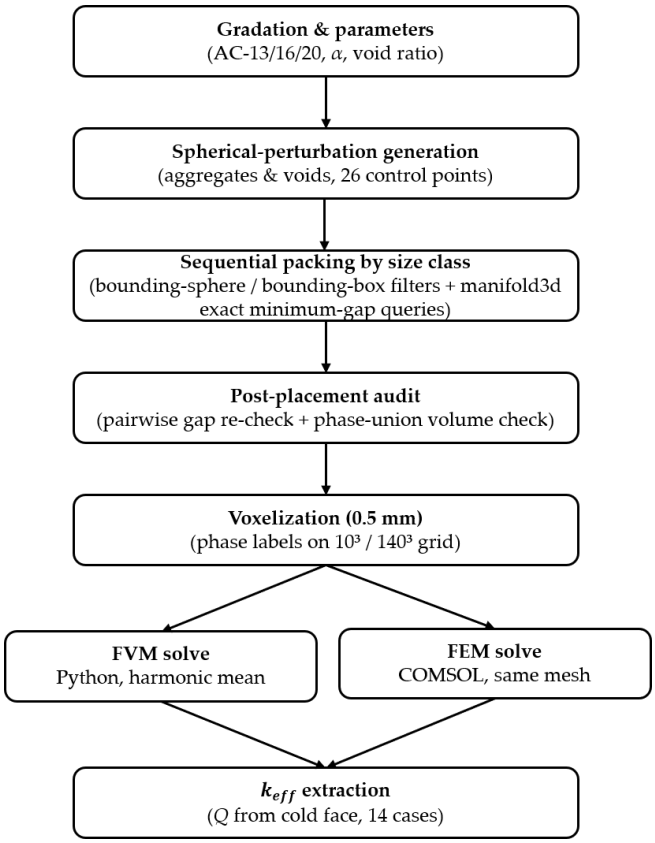


Figure 2. Overview of the modeling and solution workflow, from gradation input to effective-conductivity extraction through particle generation, packing, auditing, voxelization, and dual FVM/FEM solution.

Use of AI-Assisted Tools: During the development of this study, AI-assisted tools (specifically, Claude Code 2.1.330) were utilized to facilitate software development, automate the orchestration of the simulation pipeline, and assist with drafting the manuscript. The authors reviewed and edited all AI-assisted content. All scientific claims, mathematical models, and numerical results presented in this work were produced and verified by the computational pipeline described in this section. The authors take full responsibility for the content and integrity of the publication.

3. Numerical Thermal Conduction Method

3.1. Governing Equations and Thermal Parameters

The steady-state heat conduction equation is solved in the three-phase domain:

$$\nabla \cdot (k \nabla T) = 0 \tag{3}$$

The steady-state assumption is justified by scale separation. Using the volume-averaged density and heat capacity from Table 1, the thermal diffusivity of the base case is $6.4 \times 10^{-7}\ \frac{m^2}{s}$, yielding relaxation times of approximately 65 min for the RVE and 2 min for an individual aggregate (based on the adopted granite diffusivity). Both are much smaller than the daily temperature cycle that dominates pavement thermal loading.

The thermal properties of each phase are listed in Table 1. The aggregate phase is assigned the properties of granitic rock, as granite is the most common aggregate mineralogy in asphalt pavements and exhibits intermediate thermal conductivity among common aggregate minerals [26]. The mortar phase, defined as the mixture of asphalt binder and fine aggregates passing the 2.36 mm sieve, uses the homogenized properties derived in

Section 2.1. The void phase is assigned the properties of quiescent air. The sensitivity of the results to these property assignments is quantified in Section 4.6.

3.2. Boundary Conditions and Effective Conductivity

A temperature difference is imposed between the two faces normal to x ($T_h = 323.15$ K at $x = 0$, $T_c = 293.15$ K at $x = L$), with the remaining faces adiabatic. The effective conductivity is extracted from the total heat flow Q through the cold face:

$$k_{\text{eff}} = \frac{QL}{A\Delta T} \tag{4}$$

with $A = L^2$. Two independent solvers compute the same problem. The first is a cell-centered finite-volume (FVM) solver implemented in Python on the voxel grid, using harmonic-mean interface conductivities and a conjugate-gradient iteration with Jacobi preconditioning (relative tolerance 10^{-8}). The second is a finite-element (FEM) solution in COMSOL Multiphysics 6.3, using first-order hexahedral elements on the same voxel grid (100^3 for the AC-13 cases; 70^3, i.e., voxels of 1.0 mm, for the AC-16/AC-20 cross-validation pairs). The mesh is written in the native COMSOL text format (.mphtxt) and imported directly, so that no geometry kernel, Boolean operation, or meshing step is performed inside the FEM software (COMSOL Multiphysics 6.3). The heterogeneous material is represented by a single material domain with spatially varying properties defined by interpolation functions sampled at the voxel centers, which reproduces the voxel phase labels exactly.

Voxelization discretizes the geometric phases: each voxel is assigned to the phase containing its center. To minimize partial-volume effects, particles spanning fewer than four voxels are resolved by 8^3 sub-sampling with majority voting. Consequently, the phase fractions used in the simulations differ slightly from the geometric fractions reported in Table 2; for instance, the voxelized void fraction is 3.44% for the 4.0% base case and 3.51% and 3.55% for the AC-16 and AC-20 cases, respectively. These voxelized fractions define the actual medium solved in all analyses of Sections 4.3–4.6 and Section 5 (0.5 mm voxels throughout).

Since both solvers operate on identical voxel geometry and phase labels, their agreement validates the solution procedure rather than the spatial discretization. The latter is validated separately by the resolution study and the layered benchmark in Section 4.1. Note that the 1.0 mm AC-16 and AC-20 runs serve solely for solver cross-validation (Table 3).

Table 3. Cross-validation of the two numerical approaches.

Case	FVM k_{eff} (W/(m·K))	FEM k_{eff} (W/(m·K))	Deviation (%)
AC-13, design 3.0%	1.5630	1.5957	2.1%
AC-13, design 3.5%	1.5501	1.5857	2.3%
AC-13, design 4%	1.5384	1.5776	2.5%
AC-13, design 4.5%	1.5270	1.5692	4.5%
AC-13, design 5%	1.5148	1.5604	3.0%
AC-13, design 5.5%	1.5022	1.5511	3.3%
AC-13, design 6%	1.4927	1.5448	3.5%
AC-13, design 8% (achieved 6.12%)	1.4896	1.5422	3.5%
AC-13, $\alpha = 0.1$	1.5637	1.6040	2.6%
AC-13, $\alpha = 0.3$	1.5155	1.5538	2.5%
AC-13, $\alpha = 0.5$	1.5037	1.5404	2.4%
AC-13, $\alpha = 0.8$	1.4672	1.5014	2.3%
AC-16 (FEM 1.0 mm)	1.5844	1.6589	4.7%
AC-20 (FEM 1.0 mm)	1.6083	1.6801	4.5%

Note: Cross-validation of the two numerical approaches. Each FVM–FEM pair shares the same voxelization: 0.5 mm for the AC-13 cases and 1.0 mm for the AC-16 and AC-20 pairs. The 0.5 mm FVM results of the AC-16 and AC-20 cases are used in the gradation analysis (Section 4.4); their 1.0 mm pairs serve for solver cross-validation only. k_{eff} values are in W/(m·K). FVM, finite-volume method; FEM, finite-element method.

To ensure reproducibility, all placement runs use a fixed random seed, except for the seed-variability cases discussed in Section 4.1, and the complete workflow (generation, packing, voxelization, and the two solvers) is provided as supplementary code in the Supplementary Materials. The pipeline exports the smooth three-phase design geometry in standard STL format (metric units; Figure 3). We also export the voxel mesh for computing all quantitative results (Figure 4). These STL geometries support interoperability with third-party meshing and finite-element tools, facilitating visualization.

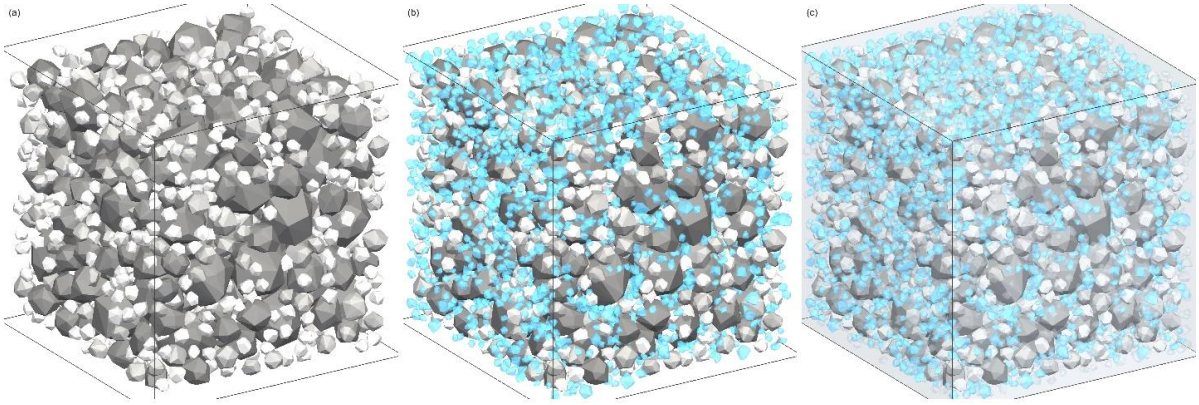


Figure 3. Construction of the base-case three-phase geometry for AC-13 (50 mm RVE) in packing sequence: (**a**) aggregate skeleton alone (1073 polyhedral aggregates; shading changes from light to dark gray with increasing particle size); (**b**) the aggregate skeleton with 3763 air voids added (light blue); (**c**) the complete three-phase geometry, with the asphalt mortar phase rendered translucent. For visualization, voids within 1.5 mm of the RVE surface are omitted to expose the internal structure.

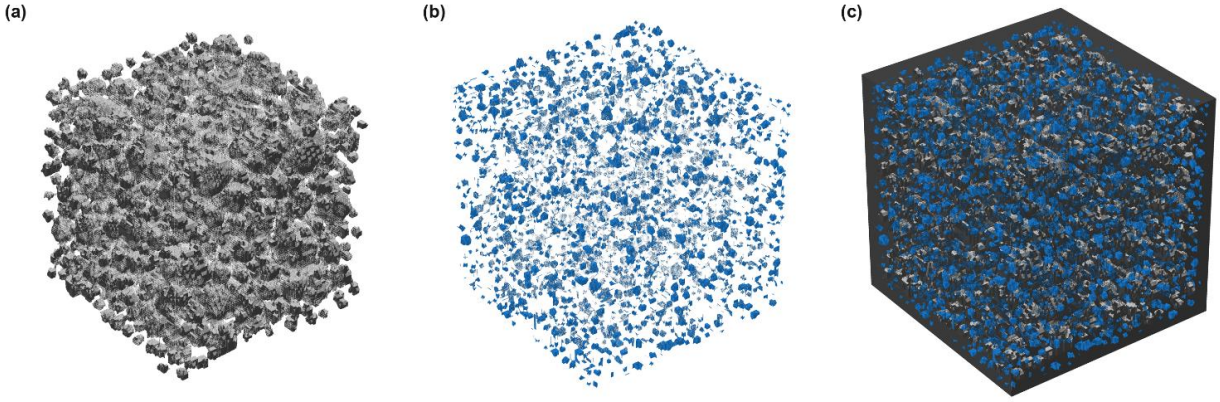


Figure 4. Volume-rendered phase decomposition of the base-case mesoscale model in COMSOL: (**a**) aggregate phase alone; (**b**) void phase alone; (**c**) asphalt mortar phase alone. All three phases rendered together using phase-specific colors (light rock-gray aggregates, bright cyan voids, and dark asphalt-gray mortar). The rendered object is the imported voxel mesh consisting of 100^3 hexahedral elements at a resolution of 0.5 mm.

4. Results

Section 4.1 establishes the numerical reliability of the computed effective conductivities through an analytical benchmark, FVM–FEM cross-validation across all 14 cases, a voxel-resolution convergence study, and seed/RVE-size sensitivity analyses. Sections 4.2–4.6 then present the mesostructural heat-flow characteristics and parametric analyses, covering the effects of air-void content, gradation, aggregate morphology, and phase thermal properties.

Finally, Section 5 discusses the Maxwell–Eucken model comparison, validations against measured data, and their engineering implications.

4.1. Numerical Reliability

Four independent checks were performed to verify the numerical reliability. First, a layered benchmark consisting of three equal-thickness slabs in series (k = 1.2, 2.8, and 0.026 W/(m·K)) has an exact analytical solution of k_{eff} = 0.0757 W/(m·K) based on the harmonic mean. Both numerical approaches reproduce this value within 0.01%. Second, the two approaches were cross-validated across all 14 cases using identical voxelizations for each FVM–FEM pair (0.5 mm for AC-13 cases and 1.0 mm for AC-16/AC-20 cases). For the twelve AC-13 cases solved at 0.5 mm, the deviations range from 2.1% to 3.5% (mean 2.7%); the AC-16 and AC-20 pairs (FEM at 1.0 mm) deviate by 4.7% and 4.5%, respectively (Table 3 and Figure 5). A Bland–Altman analysis of the 14 pairs yields a bias of +0.046 W/(m·K) (FEM higher) with 95% limits of agreement of +0.021 to +0.071 W/(m·K) and a Pearson correlation of r = 0.97. This discrepancy is on the same order of magnitude as the intrinsic discretization difference between the two methods at material interfaces, and it exhibits a slight increase with void content.

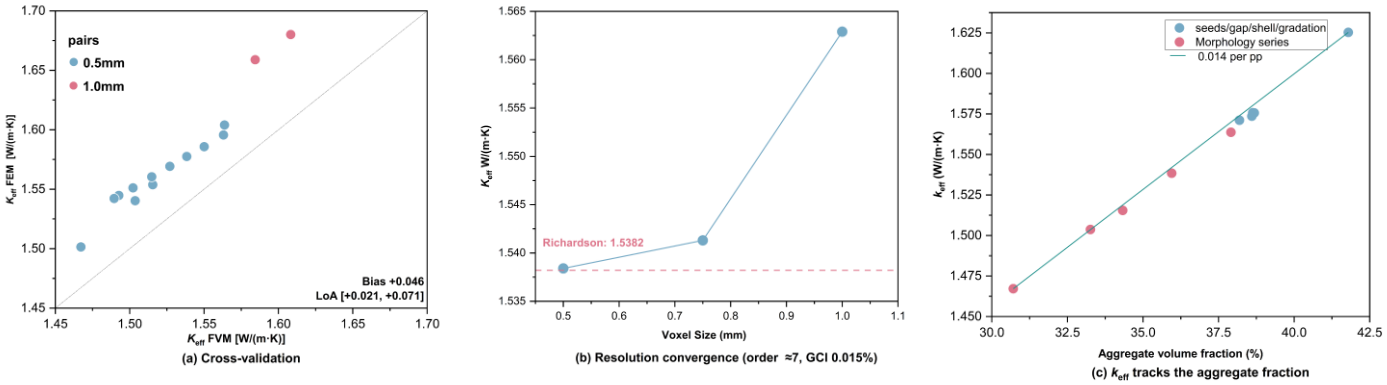


Figure 5. Reliability checks: (**a**) FVM–FEM cross-validation for the 14 cases (bias +0.046 W/(m·K), 95% limits of agreement +0.021 to +0.071 W/(m·K)); (**b**) voxel-resolution convergence with Richardson extrapolation (apparent order ≈ 7, GCI 0.015%); (**c**) sensitivity of k_{eff} to the achieved aggregate fraction across the seed, gap, shell, and gradation datasets (≈0.014 W/(m·K) per percentage point; morphology series 0.012).

Third, a voxel-resolution study of the base case yields k_{eff} values of 1.5384, 1.5413, and 1.5629 W/(m·K) for voxel sizes of 0.5, 0.75, and 1.0 mm, respectively. The difference between the two finest resolutions is only 0.19%. A Richardson extrapolation of the three resolutions gives an apparent order of ≈7, a grid convergence index of 0.015% between the 0.5 and 0.75 mm solutions, and an extrapolated converged value of 1.5382 W/(m·K), confirming convergence at 0.5 mm. Fourth, the statistical representativeness of the RVE was examined. Across five independent random placements (seeds 42–45 and 123–124), k_{eff} ranges from 1.534 to 1.576 W/(m·K). This spread is not a representativeness problem: it follows directly from the spread of the achieved aggregate fraction (35.9–38.7%), because k_{eff} changes by about 0.014 W/(m·K) for every percentage point of aggregate fraction. The same sensitivity is recovered from the gap-sensitivity, shell-removal, and same-RVE-size gradation datasets, whereas the morphology series yields 0.012, the difference being the direct shape effect beyond packing. Removing the 0.6 mm mortar shell raises the achieved aggregate fraction by 5.8 percentage points and k_{eff} by 5.7%; only ≈0.5% of this change remains when the composition is held fixed, so the shell matters chiefly through the packing it constrains. Solving AC-16 in the same 50 mm RVE gives

k_{eff} = 1.574 W/(m·K) at 38.6% aggregate: the AC-13-to-AC-16 difference at fixed RVE size is therefore fully explained by composition, and the residual RVE-size effect (50 vs. 70 mm) is only 0.7%, consistent with the 1.1% estimate above. Varying the RVE size from 40 to 60 mm changes k_{eff} by 1.1% (1.529 and 1.546 W/(m·K)), which brackets the 50 mm value of 1.538 W/(m·K). Both variations are significantly smaller than the parametric effects reported in Section 4, confirming the representativeness of the adopted RVE sizes. Two additional checks complete the microstructure-level reliability picture. (i) Isotropy: solving the base case along the three principal axes gives k_{eff} = 1.5384, 1.5388, and 1.5368 W/(m·K) (directional spread 0.13%), confirming that the generated microstructure is effectively isotropic. (ii) Gap sensitivity: re-packing the base case with a fixed 0.10 mm minimum surface gap (instead of the 0.20 mm initial value with a 0.10 mm floor) increases k_{eff} by 2.4% (1.5757 vs. 1.5384 W/(m·K)), accompanied by an increase in the achieved aggregate fraction from 35.95% to 38.63%, indicating that the gap choice acts chiefly through the achievable packing rather than through the film physics at fixed composition.

4.2. Mesostructural Temperature and Heat-Flow Characteristics

Figure 3 shows the three-phase RVE for the base case, containing 1073 polyhedral aggregates (35.95% volume fraction) and 3763 air voids (4.0%) embedded in an asphalt mortar matrix. Figure 6 displays the computed temperature field on a central slice, and Figure 4 presents the volume-rendered phase decomposition in COMSOL. The temperature field decreases monotonically from the hot to the cold face, exhibiting local distortions at phase interfaces: the temperature gradient steepens inside the voids and flattens inside the aggregates.

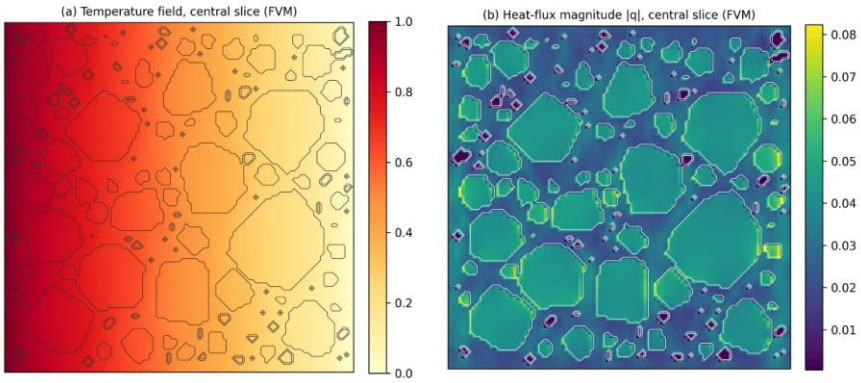


Figure 6. (**a**) Temperature field and (**b**) heat-flux magnitude on the central slice of the base case (FVM, 0.5 mm voxels, 1 K applied along the x-axis), with phase boundaries overlaid. The isotherm distortion at aggregate and void interfaces reflects the influence of the two phases on the local temperature gradient z = 25.

Heat flows preferentially along chains of nearly touching aggregates separated by thin mortar films. Two notable features emerge from the results. First, these percolating aggregate bridges are a geometric feature of the packing; chains of large particles (9.5–16 mm) span the RVE along the temperature gradient with a mean nearest-surface distance below 0.2 mm. The highest interfacial heat fluxes occur at the narrowest mortar films between adjacent large aggregates. The modest net contribution of this channel structure to k_{eff} is quantified in Section 4.4. Second, voids interrupt the mortar matrix or these bridges, acting as local insulators. This tendency to occupy the free space between aggregates is effectively captured by the distance-field-guided packing algorithm. These observations link the effective property to local geometric features and motivate the parametric analyses in the following sections.

4.3. Effect of Air-Void Content

Figure 7 presents k_{eff} as a function of the achieved air-void content. Over the range of 3.0% to 6.1% (comprising eight points at 0.5 percentage-point intervals up to 6.0%, plus a maximum-achievable case of 6.12%), k_{eff} decreases by approximately 0.024 W/(m·K) per percentage point of void content for the FVM approach (about 1.5% per percentage point, with a linear fit of $R^2 = 0.999$). For the FEM approach, the decrease is 0.017 W/(m·K) per percentage point. The analytical model follows the same trend as the numerical solutions. The decline remains approximately linear, without any plateau or saturation over the entire range. This series covers the 3–6% design air-void interval for dense-graded asphalt mixtures (i.e., the 4% AASHTO Superpave design target [22] and the EN 13108-1 void-content classes [25]). Importantly, it extends to levels above 6%, which are common under Superpave field compaction.

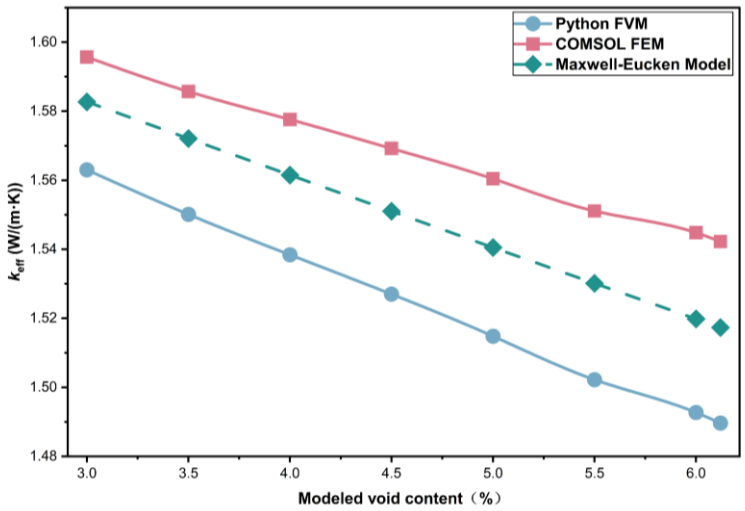


Figure 7. Effective thermal conductivity (k_{eff} versus modeled air-void content for the two numerical approaches (FVM and FEM) and the analytical Maxwell–Eucken model.

4.4. Effect of Aggregate Gradation

To isolate the effect of gradation, the three mixtures were compared at comparable aggregate volume fractions (36–41%) and a uniform air-void content of 4.0%. Figure 8 plots k_{eff} for the three gradations. The computed k_{eff} increases from AC-13 (1.538 W/(m·K)) to AC-16 (1.584 W/(m·K)) to AC-20 (1.608 W/(m·K)), spanning a range of 4.5%. The gradation series uses the 0.5 mm FVM results; the FEM values listed for AC-16 and AC-20 in Table 3 are at 1.0 mm and serve for solver cross-validation only. Under the same placement budget, coarser gradations achieve higher aggregate volume fractions (36.0%, 39.5%, and 41.1%, respectively). When substituting the phase fractions of each case into the Maxwell–Eucken model, the predicted span is 4.3–4.5% (depending on whether voxelized or geometric fractions are used), which covers essentially the entire simulated variation.

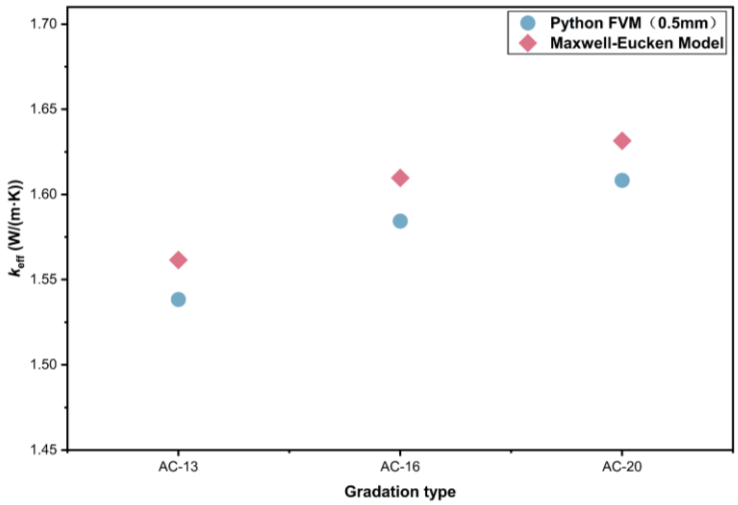


Figure 8. Effective thermal conductivity (k_{eff}) of the three gradations obtained from the FVM approach (0.5 mm) and the analytical Maxwell–Eucken model, with the achieved aggregate volume fractions annotated.

4.5. Effect of Aggregate Morphology

Figure 9 presents the effective thermal conductivity (k_{eff}) for the morphology series. As the perturbation coefficient α increases from 0.1 to 0.8, the achievable aggregate volume fraction decreases monotonically from 37.9% to 30.7% under a constant design air-void content of 4.0%. Correspondingly, k_{eff} decreases from 1.564 to 1.467 W/(m·K) for the FVM approach.

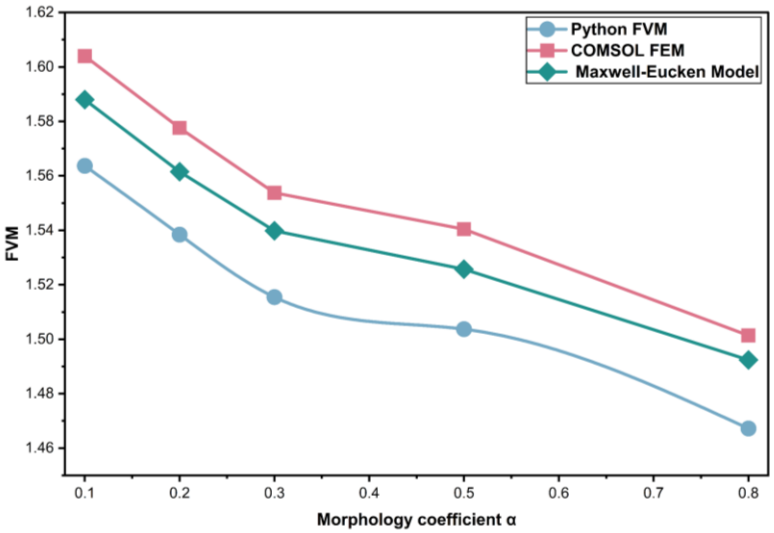


Figure 9. Effective thermal conductivity (k_{eff}) versus the morphology coefficient for the AC-13 series, obtained from the two numerical approaches (FVM and FEM) and the analytical Maxwell–Eucken model.

A similar decreasing trend is observed in the FEM simulations, where k_{eff} drops from 1.604 to 1.501 W/(m·K) over the same α range, maintaining a consistent deviation from the FVM results as discussed in Section 4.1. The analytical Maxwell–Eucken model, utilizing the achieved phase fractions of each case, also closely tracks this downward trend. Notably, the most significant drop in k_{eff} occurs between $\alpha = 0.1$ and $\alpha = 0.3$, which corresponds to the sharpest decline in the achievable aggregate volume fraction within this series.

4.6. Sensitivity to Phase Thermal Properties

Figure 10 reports the sensitivity of k_{eff} to the phase thermal conductivities for the base-case geometry (baseline $k_{\text{eff}} = 1.538$ W/(m·K)). The results indicate that the mortar phase is the most influential parameter. When k_{mat} is varied by ±33%, k_{eff} shifts significantly, ranging from a 22.5% reduction to a 19.4% increase. The aggregate conductivity ranks second in influence. Decreasing k_{agg} from its baseline of 2.8 to 1.5 W/(m·K) lowers k_{eff} by 21.1%, whereas increasing it to 4.0 W/(m·K) raises k_{eff} by 14.1%. In comparison, the downward sensitivity to the aggregate conductivity is stronger than the upward sensitivity at the studied bounds.

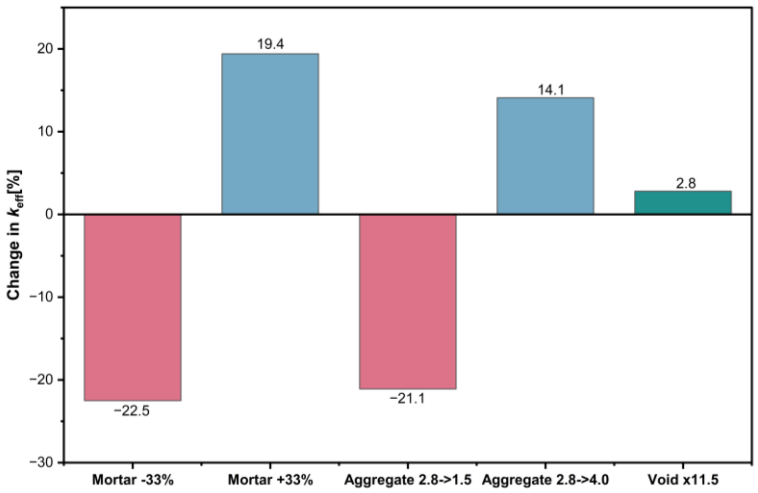


Figure 10. Sensitivity of the effective thermal conductivity (k_{eff}) to the phase conductivities for the base-case geometry using the FVM approach: change in k_{eff} induced by each phase-conductivity variation.

Regarding the void phase, the baseline radiative transfer was estimated from $k_{\text{rad}} = 4\varepsilon\sigma T^3 d$ to be approximately 0.019 W/(m·K) for 2.5 mm voids at 60 °C. To test the extreme case, a deliberately exaggerated void conductivity of 0.3 W/(m·K) (about 11.5 times the baseline value) was assigned, which resulted in an increase in k_{eff} of only 2.8%. The variation caused by the void phase is thus the smallest among all three phases.

5. Discussion

5.1. Physical Mechanisms of Heat Conduction

The mesostructural results reveal that heat flows preferentially along percolating aggregate bridges. This occurs because the aggregate phase has a significantly higher thermal conductivity than the mortar matrix, creating a path of least resistance for heat transfer. Conversely, voids act as local insulators because of their extremely low conductivity; when they interrupt the narrow mortar films between aggregates, they severely restrict the primary conduction channels. This insulating action stems not only from their low conductivity but also from their preferential placement. The distance-field-guided algorithm inserts voids in a way that maximizes the reduction per unit void volume, which is consistent with experimental findings that void content, rather than void connectivity, governs the thermal effect [27].

Similarly, the morphology series reveals a coupled morphological mechanism. Rougher particles pack less efficiently under the same placement algorithm, yielding a looser aggregate skeleton. The generated sphericities (0.86–0.94) may lie above those of strongly angular crushed aggregates, so the packing penalty quantified here likely represents a lower bound for such materials; the ±20° angular perturbation is kept independent of α so that

the radial and angular shape descriptors remain orthogonal. The sequential placement algorithm could in principle exaggerate the packing penalty of rough particles, but because the identical algorithm and placement budget are applied to all morphology levels, the comparative trend remains meaningful. Because the air-void content is held constant at 4.0%, the resulting reduction in the aggregate volume fraction accounts for the dominant part of the decrease in k_{eff}, whereas the direct contribution of interface tortuosity at a fixed composition is comparatively minor. This morphology–packing–conduction chain is consistent with the packing-density dependence of thermal conductivity observed in particulate composites [28,29]. It also aligns with the sphericity and orientation effects reported for Voronoi-based aggregate models [7], as well as the coupled effects of aspect ratio and orientation identified by Chen et al. [5]. This coupling implies that, in real mixtures, morphology effects cannot be decoupled from their compaction consequences; therefore, morphology and compaction cannot be varied independently. It is precisely this interaction that the present unified framework quantifies.

5.2. Compositional Dominance and Phase Sensitivity

A flux analysis of the FVM solution quantifies this picture (Figure 6b). The aggregate phase carries a mean heat flux 1.5 times the domain average (maximum ≈ 3 times), confirming that aggregates act as preferred conduction paths; the mortar films between adjacent aggregates carry a mean flux of 0.82 times the domain average, i.e., no flux magnification of the kind that a percolating aggregate skeleton would produce; and the void phase carries only ≈3% of the domain-average flux, so heat routes around voids rather than through them. This is consistent with the simulated conductivity (1.538) lying slightly below the mortar-continuous Maxwell–Eucken prediction (1.562): the aggregate skeleton at the achieved volume fraction shortens the effective path through the mortar but does not form a continuous high-conductivity network, and the distance to the Hashin–Shtrikman upper bound quantifies the margin that such a network would provide.

The gradation effect operates almost entirely through the phase composition it produces. The size distribution alters the packing efficiency and thus the phase fractions, whereas the direct geometric contribution of the continuous large-particle bridge chains in coarser gradations is negligible at the resolutions studied. Consequently, the gradation effect is predominantly compositional at the studied aggregate volume fractions. A direct comparison with measurements is not straightforward: the transient plane source (TPS) study by Khasawneh et al. [30] reported higher conductivity for finer gradations at a fixed target air-void content. That result was likely dominated by the higher effective binder content of fine-graded mixtures rather than by the aggregate size distribution itself. In contrast, the present simulations hold the air-void content and phase properties fixed across gradations, thereby isolating the geometric effect of the size distribution.

The sensitivity analysis further reveals a clear hierarchy of phase properties. The aggregate-source dependence observed in Section 4.6 is consistent with the experimental measurements for basalt versus dolomite mixtures [20]. The strong binder sensitivity also indicates the potential of binder modification for thermally functional pavements: nano-alumina modification has been shown to raise binder conductivity progressively with dosage [31], phase-change modification offers a parallel route that also alters mixture thermophysical properties [32], and pavement-temperature modeling indicates that such conductivity gains measurably reduce surface temperatures [33]. Expressed as logarithmic elasticities ($\frac{\partial \ln k_{\text{eff}}}{\partial \ln k_i}$), the mortar (≈0.63) outranks the aggregate (≈0.38), with the void phase far behind (≈0.01). This phase-level ranking is consistent with the experimental finding that aggregate mineralogy influences mixture conductivity more than binder content [26,34]: the mortar conductivity is itself a homogenized property of the binder and fine fraction,

whereas the aggregate phase combines a large volume fraction with a wide mineralogical conductivity span. Furthermore, the minimal impact of the exaggerated void conductivity confirms that radiative transfer can be safely neglected in dense-graded mixtures at typical pavement temperatures. This ranking of influential parameters—where the continuous matrix (mortar) and aggregate dominate while void radiation is negligible—agrees well with the experimental finding that aggregate mineralogy is more influential than binder content [26,34] and with previous numerical sensitivity studies on concrete [29].

5.3. Analytical Model Validation and Engineering Application

The simulation results are compared with the generalized Maxwell–Eucken model in the Maxwell–Garnett form [35,36], where the mortar is the continuous matrix and the aggregates and voids are treated as spherical inclusions [10,11]:

$$k_{\text{eff}} = k_{mat}\frac{1 + 2\sum_i \varphi_i \beta_i}{1 - \sum_i \varphi_i \beta_i}, \quad \beta_i = \frac{k_i - k_{mat}}{k_i + 2k_{mat}} \tag{5}$$

The single-step multi-inclusion form is adopted instead of sequential homogenization because the generalized form is provably independent of the embedding order and follows directly from Maxwell's far-field methodology for multiphase composites [10,37]. The predictive accuracy of this model is demonstrated in Figure 11. Inserting the phase fractions of the 3.0% and 6.1% endpoints into the Maxwell–Eucken expression predicts a decrease of 0.065 W/(m·K), accounting for approximately 89% of the simulated decrease of 0.073 W/(m·K). Using voxelized phase fractions, the model reproduces the FVM results with a mean deviation of 2.4% (maximum 3.6%) and the FEM results with 0.5% (maximum 2.3%); with the geometric phase fractions the corresponding statistics are 1.6% (maximum 1.9%) against FVM and 1.3% (maximum 3.0%) against FEM. Table 4 summarizes all four comparisons across the 14 cases, resolving the previous reporting inconsistencies. All deviations fall within ±5%. The slightly flatter trend observed in the FEM approach compared to the FVM approach reflects the gradual accumulation of discretization errors near voids in contact with aggregates, as noted in Section 4.1.

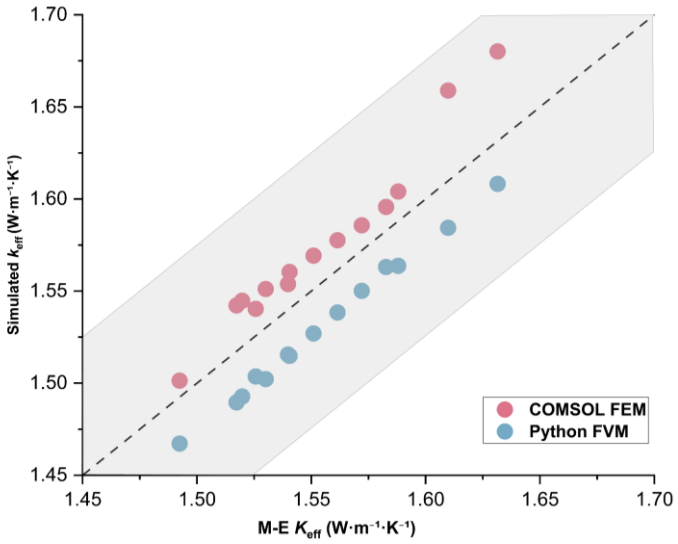


Figure 11. Parity plot of the Maxwell–Eucken model against the simulated effective thermal conductivities. The shaded band indicates ±5%. Using geometric phase fractions, the mean deviations are 1.6% for FVM and 1.1% for FEM. And the dashed diagonal line represents the 1:1 line (perfect agreement).

Table 4. Summary of Maxwell–Eucken deviations from the numerical results (14 cases): geometric fractions, mean/max 1.6%/1.9% vs. FVM and 1.3%/3.0% vs. FEM; voxelized fractions, 2.4%/3.6% vs. FVM and 0.5%/2.3% vs. FEM.

Case	FVM k_{eff}	FEM k_{eff}	ME (Geometric Fractions)	Dev. vs. FVM (%)	Dev. vs. FEM (%)	ME (Voxelized Fractions)	Dev. vs. FVM (%)	Dev. vs. FEM (%)
AC-13, design 3.0%	1.5630	1.5957	1.5827	+1.3	−0.8	1.5898	+1.7	−0.4
AC-13, design 3.5%	1.5501	1.5857	1.5721	+1.4	−0.9	1.5810	+2.0	−0.3
AC-13, alpha = 0.1	1.5637	1.6040	1.5880	+1.6	−1.0	1.6013	+2.4	−0.2
AC-13, design 4%	1.6083	1.6801	1.6315	+1.4	−2.9	1.6414	+2.1	−2.3
AC-13, alpha = 0.3	1.5155	1.5538	1.5398	+1.6	−0.9	1.5509	+2.3	−0.2
AC-13, alpha = 0.5	1.5037	1.5404	1.5257	+1.5	−1.0	1.5350	+2.1	−0.3
AC-13, alpha = 0.8	1.4672	1.5014	1.4924	+1.7	−0.6	1.5003	+2.3	−0.1
AC-13, design 4.5%	1.5270	1.5692	1.5510	+1.6	−1.2	1.5660	+2.6	−0.2
AC-13, design 5%	1.5148	1.5604	1.5405	+1.7	−1.3	1.5584	+2.9	−0.1
AC-13, design 5.5%	1.5022	1.5511	1.5301	+1.9	−1.4	1.5510	+3.2	−0.0
AC-13, design 6%	1.4927	1.5448	1.5198	+1.8	−1.6	1.5445	+3.5	−0.0
AC-13, design 8% (achieved 6.12%)	1.4896	1.5422	1.5173	+1.9	−1.6	1.5426	+3.6	+0.0
AC-16	1.5844	1.6589	1.6098	+1.6	−3.0	1.6203	+2.3	−2.3
AC-20	1.6083	1.6801	1.6315	+1.4	−2.9	1.6414	+2.1	−2.3

Two caveats should be considered when interpreting this agreement. First, the comparison assesses the agreement between the model and numerical solutions, not experiments. Deviations of the bare Maxwell–Eucken model from measured mixture conductivities reported in the literature are substantially larger (on the order of 30%) and are dominated by interfacial thermal resistance [28,38]. Second, the topology assumption warrants examination: assigning the reference conductivity to the least conductive phase (voids) or the most conductive phase (aggregate) reproduces the Hashin–Shtrikman lower and upper bounds, respectively [11,12,29]. For the base case, these bounds are 0.842 and 1.635 W/(m·K), and the mortar-continuous choice adopted here yields 1.562 W/(m·K). This lies between the bounds and is close to the simulated 1.538 W/(m·K). This agreement indicates a mortar-continuous heat-flow topology, while the distance to the upper bound quantifies the margin available if the aggregate skeleton were fully continuous.

The spherical-shape approximation is acceptable because particle shape factors affect mixture conductivity far less than interfacial thermal resistance does [38]. Within the studied composition range, the analytical expression can be used directly for engineering prediction; outside this range, an interfacial-resistance correction should be added [28,38]. Combined with the sensitivity ranking in Figure 10, this provides a two-step design procedure: first, select the aggregate mineralogy; then, adjust the gradation and compaction target within the conductivity range bounded by the lower and upper bounds.

Finally, the numerical model was benchmarked against measured data from the literature (Figure 12). The simulated k_{eff} over the studied composition space (3.0–6.1% air-void contents) ranges from 1.47 to 1.61 W/(m·K) (FVM, 0.5 mm voxels) and lies within the 1.4–1.8 W/(m·K) range reported for dense-graded Superpave mixtures [1]. Measurements on mixtures with high-conductivity aggregates (dolomite and quartzite) range from 1.7 to 2.45 W/(m·K) [20,26], consistent with the k_{agg} sensitivity. Transient plane source (TPS) measurements for diabase mixtures [39], obtained with the ISO 22007-2 hot-disc method [40], are systematically about 10% higher than steady-state equivalents [41]; a recent controlled comparison likewise finds that TPS overestimates mixture conductivity relative to steady-state heat-flux measurements [42]. After correcting for this overestimation, the values fall below the simulated range, which is expected due to the lower thermal conductivity of diabase relative to granite. Within these bounds, the simulated values are consistent with the measured range, supporting the adopted phase properties as a quantitative basis for thermal design.

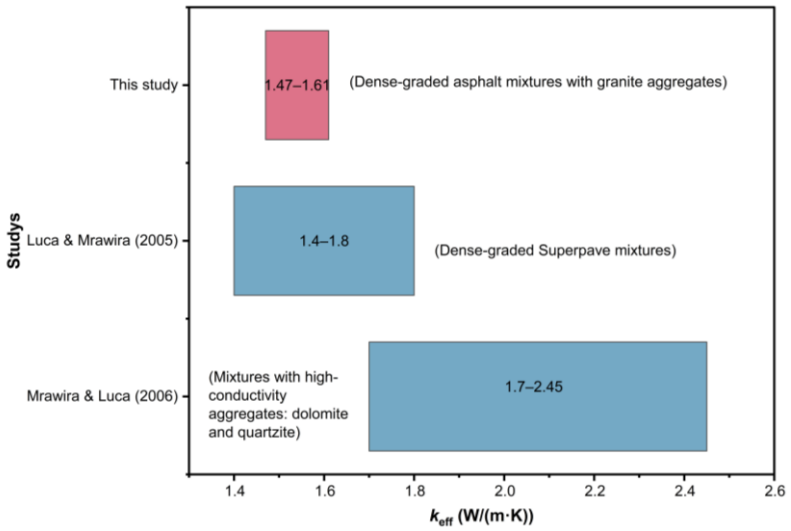


Figure 12. Comparison of the simulated and measured effective thermal conductivity ranges for dense-graded asphalt mixtures, with the aggregate composition and mineralogy of each study annotated. The simulated range (1.47–1.61 W/(m·K), FVM, 0.5 mm voxels, granite aggregates) falls within the range reported for dense-graded Superpave mixtures [1] and below the range of dolomite- and quartzite-aggregate mixtures [20,26].

6. Conclusions

A unified parametric mesoscale modeling framework for the thermal conduction of asphalt mixtures was developed and numerically verified using two independent approaches. The principal findings are as follows:

- The Python FVM and COMSOL FEM approaches agree within 2.1–3.5% (mean 2.7%) for the twelve 0.5 mm AC-13 pairs (4.7% and 4.5% for the two 1.0 mm gradation pairs) and reproduce the analytical layered benchmark within 0.01%; a voxel-resolution study confirms convergence at 0.5 mm. The pipeline requires no geometry repair inside the FEM software, resolving a practical reliability bottleneck of mesoscale simulation.
- The simulated effective thermal conductivity ranges from 1.47 to 1.61 W/(m·K) (FVM, 0.5 mm voxels) over the studied composition space and lies within the measured range for dense-graded mixtures, supporting the adopted phase properties as a reliable baseline for numerical analysis.
- The air-void content series covers the 3–6% design air-void interval of dense-graded mixtures (the 4% Superpave design target [22] and the EN 13108-1 void-content classes [25]) with 6.12% the maximum achieved value: k_{eff} decreases approximately linearly with air-void content at 0.024 W/(m·K) per percentage point with no sign of saturation, and a Maxwell–Eucken expression reproduces about 89% of this reduction.
- Aggregate morphology acts on conduction chiefly through packing: at a fixed air-void content of 4.0%, rougher aggregates reduce the achievable aggregate volume fraction, thereby lowering k_{eff}. This morphology–packing–conduction chain shows that the shape effect operates chiefly through packing efficiency, consistent with the close ($\leq$3.0%) agreement of the spherical-inclusion Maxwell–Eucken model with all simulations.
- A generalized Maxwell–Eucken expression reproduces all numerical results within 3.0% and shows promise as a simplified engineering prediction tool. However, its absolute predictive accuracy against physical experiments requires further validation. Within the studied composition range, it can serve as a rapid estimation method; outside this range, an interfacial-resistance correction is advised.

Limitations: the study covers a single aggregate mineralogy and fixed phase properties, except where these were varied in the sensitivity analysis. The mortar homogenization adopts the asphalt-phase value of 0.75 W/(m·K) from mesoscale homogenization practice [4]; this value exceeds some neat-binder measurements (≈0.2 W/(m·K)), and its influence on k_{eff} is bounded by the ±33% mortar sweep in Section 4.6. The achieved aggregate volume fractions (31–41%) lie below the design targets because the exact-gap constraint and the placement procedure limit the attainable packing; mixtures compacted to higher aggregate contents fall outside the validated composition range. The void size window (1.0–2.5 mm) captures only part of the measured void population, and sub-voxel features are discretized by the 0.5 mm grid. Transient thermal behavior, moisture, and coupled radiative effects at high temperatures remain topics for future work.

Supplementary Materials: The following supporting information can be downloaded at: https://www.mdpi.com/article/10.3390/ma19234999/s1.

Author Contributions: S.H. contributed to the conceptualization, methodology, software development, formal analysis, and writing the original draft. J.Z. contributed to data curation, literature collection and verification, and visualization. D.Y. (corresponding author) contributed to supervision, project administration, funding acquisition, and review and editing. All authors have read and agreed to the published version of the manuscript.

Funding: This research was funded by the Key Research and Development Program of Shaanxi, grant number 2026SF-YBXM-165; and the Fundamental Research Funds for Central Universities, grant number CHD 300102215103.

Institutional Review Board Statement: Not applicable.

Informed Consent Statement: Not applicable.

Data Availability Statement: The datasets generated during and/or analyzed during the current study are available from the corresponding author on reasonable request. The complete numerical workflow (including particle generation, packing, voxelization, and the two solvers) is provided as supplementary code.

Acknowledgments: The authors would like to express their sincere gratitude to Yuan for his valuable guidance and supervision throughout this research. This work was supported by the College Students' Innovation and Entrepreneurship Training Program. The authors also appreciate the School of Highway, Chang'an University for its academic support. Special thanks are extended to Shuangning Liu for her meticulous assistance in language polishing and translation. During the preparation of this work, AI-assisted tools (Claude Code 2.1.330) were used for software development, automated simulation orchestration, drafting assistance, and language polishing. All scientific claims and numerical results were produced by the computational pipeline described in Section 3; every reference was checked against publisher records during revision. The authors reviewed and edited the AI-assisted content as needed and take full responsibility for the content of the publication. All authors have read and agreed to the published version of the manuscript.

Conflicts of Interest: The authors declare no conflicts of interest.

References

1. Luca, J.; Mrawira, D. New Measurement of Thermal Properties of Superpave Asphalt Concrete. *J. Mater. Civ. Eng.* **2005**, *17*, 72–79. [CrossRef]
2. Côté, J.; Grosjean, V.; Konrad, J. Thermal Conductivity of Bitumen Concrete. *Can. J. Civ. Eng.* **2013**, *40*, 172–180. [CrossRef]
3. Byzyka, J.; Rahman, M.; Chamberlain, D. A Laboratory Investigation on Thermal Properties of Virgin and Aged Asphalt Mixture. *Constr. Build. Mater.* **2021**, *305*, 124757. [CrossRef]
4. Chen, J.; Wang, H.; Li, L. Determination of Effective Thermal Conductivity of Asphalt Concrete with Random Aggregate Microstructure. *J. Mater. Civ. Eng.* **2015**, *27*, 04015045. [CrossRef]

5. Chen, J.; Zhang, M.; Wang, H.; Li, L. Evaluation of Thermal Conductivity of Asphalt Concrete with Heterogeneous Microstructure. *Appl. Therm. Eng.* **2015**, *84*, 368–374. [CrossRef]
6. Wriggers, P.; Moftah, S. Mesoscale Models for Concrete: Homogenisation and Damage Behaviour. *Finite Elem. Anal. Des.* **2006**, *42*, 623–636. [CrossRef]
7. Zhang, L.; Wang, H.; Ren, Z. Computational Analysis of Thermal Conductivity of Asphalt Mixture Using Virtually Generated Three-Dimensional Microstructure. *J. Mater. Civ. Eng.* **2017**, *29*, 04017234. [CrossRef]
8. Zhao, Y.; Jiang, J.; Dai, Y.; Zhou, L.; Ni, F. Thermal Property Evaluation of Porous Asphalt Concrete Based on Heterogeneous Meso-structure Finite Element Simulation. *Appl. Sci.* **2020**, *10*, 1671. [CrossRef]
9. Tong, Y.; Gu, H.; Lao, Q.; Yang, K.; Li, B.; Yang, W.; Geng, Y. Investigation of Heat Transfer Performance of Asphalt Pavements at Different Compaction Levels Based on CT Reconstruction. *Case Stud. Constr. Mater.* **2026**, *24*, e05994. [CrossRef]
10. Myles, T.; Peracchio, A.; Chiu, W. Extension of Anisotropic Effective Medium Theory to Account for an Arbitrary Number of Inclusion Types. *J. Appl. Phys.* **2015**, *117*, 025101. [CrossRef]
11. Wang, J.; Carson, J.; North, M.; Cleland, D. A New Approach to Modelling the Effective Thermal Conductivity of Heterogeneous Materials. *Int. J. Heat Mass Transf.* **2006**, *49*, 3075–3083. [CrossRef]
12. Hashin, Z.; Shtrikman, S. A Variational Approach to the Theory of the Effective Magnetic Permeability of Multiphase Materials. *J. Appl. Phys.* **1962**, *33*, 3125–3131. [CrossRef]
13. Bruggeman, D.A.G. Berechnung verschiedener physikalischer Konstanten von heterogenen Substanzen. I. Dielektrizitätskonstanten und Leitfähigkeiten der Mischkörper aus isotropen Substanzen. *Ann. Phys.* **1935**, *416*, 636–664. [CrossRef]
14. Nielsen, L.E. Thermal Conductivity of Particulate-Filled Polymers. *J. Appl. Polym. Sci.* **1973**, *17*, 3819–3820. [CrossRef]
15. Chu, L.; He, L.; Fwa, T. 3-Dimensional Finite Element Modelling of Asphalt Mixtures for Thermal Conductivity Determination. *Int. J. Pavement Eng.* **2022**, *23*, 2009–2018. [CrossRef]
16. Sha, X. Meso-Structure Study on Thermal Conductivity of Grouting Asphalt Concrete. *China Meas. Test* **2024**, *50*, 120–125. [CrossRef]
17. Fan, S.; Zhu, H.; Mou, X.; Zhang, W.; Gan, X. 3D Heterogeneous Model Created using Computer-generated Algorithm for Evaluating Thermophysical Parameters of Asphalt Mixtures. *Constr. Build. Mater.* **2025**, *479*, 141499. [CrossRef]
18. Wang, F.; Ren, Z.; Liu, K.; Yang, Z. A Mathematical Prediction Model for Calculating the Thermal Conductivity of the Asphalt Mixture. *Mater. Struct.* **2023**, *56*, 143. [CrossRef]
19. Torquato, S. *Random Heterogeneous Materials: Microstructure and Macroscopic Properties*; Springer: New York, NY, USA, 2002.
20. Demirtürk, D.; Ozturk, H.; Guler, M. Investigation of the Influence of Mixture and Microstructural Properties on the Thermal Conductivity of Asphalt Concrete using the Transient Heat Transfer Method. *Mater. Struct.* **2024**, *57*, 179. [CrossRef]
21. *JTG F40-2004*; Technical Specifications for Construction of Highway Asphalt Pavements. Ministry of Transport of the People's Republic of China: Beijing, China, 2004.
22. *AASHTO M 323-22*; Standard Specification for Superpave Volumetric Mix Design. American Association of State Highway and Transportation Officials: Washington, DC, USA, 2022.
23. Cominsky, R.; Huber, G.; Kennedy, T.; Anderson, M. *The Superpave Mix Design Manual for New Construction and Overlays*; SHRP-A-407; Strategic Highway Research Program, National Research Council: Washington, DC, USA, 1994.
24. *AASHTO R 35-22*; Standard Practice for Superpave Volumetric Design for Asphalt Mixtures. American Association of State Highway and Transportation Officials: Washington, DC, USA, 2022.
25. *EN 13108-1:2016*; Bituminous Mixtures—Material Specifications—Part 1: Asphalt Concrete. European Committee for Standardization: Brussels, Belgium, 2016.
26. Mrawira, D.; Luca, J. Effect of Aggregate Type, Gradation, and Compaction Level on Thermal Properties of Hot-mix Asphalts. *Can. J. Civ. Eng.* **2006**, *33*, 1410–1417. [CrossRef]
27. Hassn, A.; Aboufoul, M.; Wu, Y.; Dawson, A.; Garcia, A. Effect of Air Voids Content on Thermal Properties of Asphalt Mixtures. *Constr. Build. Mater.* **2016**, *115*, 327–335. [CrossRef]
28. Zhang, W.; Min, H.; Gu, X.; Xi, Y.; Xing, Y. Mesoscale Model for Thermal Conductivity of Concrete. *Constr. Build. Mater.* **2015**, *98*, 8–16. [CrossRef]
29. Carson, J.; Lovatt, S.; Tanner, D.; Cleland, A. Thermal Conductivity Bounds for Isotropic, Porous Materials. *Int. J. Heat Mass Transf.* **2005**, *48*, 2150–2158. [CrossRef]
30. Khasawneh, M.; Sawalha, A.; Aljarrah, M.; Alsheyab, M. Effect of Aggregate Gradation and Asphalt Mix Volumetrics on the Thermal Properties of Asphalt Concrete. *Case Stud. Constr. Mater.* **2023**, *18*, e01725. [CrossRef]
31. Broering, W.B.; de Melo, J.V.S.; Manfro, A.L. Modification of the Asphalt Binder with Nano-Aluminum Oxide: An Alternative to Improve the Thermal Conductivity and the Rheological Properties of the Asphalt Matrix. *J. Test. Eval.* **2024**, *52*, 1109–1128. [CrossRef]
32. Li, S.; Tan, Y.; Fu, Y.; Li, J.; Ye, W.; Li, G.; Liu, X. Effect of Phase Change Materials on Thermophysical Properties of Asphalt Mixtures and Snow Melting Performance. *Constr. Build. Mater.* **2024**, *438*, 136968. [CrossRef]

33. Dogani Aghcheghloo, P.; Larkin, T.; Wilson, D.; Holleran, G.; Amirpour, M.; Kim, S.; Bickerton, S.; Covic, G. The Effect of an Emulator Inductive Power Transfer Pad on the Temperature of an Asphalt Pavement. *Constr. Build. Mater.* **2023**, *392*, 131783. [CrossRef]
34. Zhang, Q.; Li, Y.; Xie, L. Test of Thermal Conductivity of Asphalt Mixture and Analysis of Its Influencing Factors. *J. Xi'an Univ. Archit. Technol. (Nat. Sci. Ed.)* **2014**, *46*, 199–203.
35. Maxwell, J.C. *A Treatise on Electricity and Magnetism*; Clarendon Press: Oxford, UK, 1873.
36. Eucken, A. Die Wärmeleitfähigkeit Keramischer Feuerfester Stoffe. *VDI-Forschungsheft* **1932**, *353*, 1–16.
37. McCartney, L.; Kelly, A. Maxwell's Far-field Methodology Applied to the Prediction of Properties of Multi-phase Isotropic Particulate Composites. *Proc. R. Soc. A* **2008**, *464*, 423–446. [CrossRef]
38. Guo, M.; Yao, X.; Fu, Y.; Du, X. Characterization of Thermophysical Parameters of Asphalt Composites and Proposal of Computing Method of Thermal Conductivity. *Therm. Sci. Eng. Prog.* **2024**, *49*, 102456. [CrossRef]
39. Mirzanamadi, R.; Johansson, P.; Grammatikos, S. Thermal Properties of Asphalt Concrete: A Numerical and Experimental Study. *Constr. Build. Mater.* **2018**, *158*, 774–785. [CrossRef]
40. *ISO 22007-2:2022*; Plastics—Determination of Thermal Conductivity and Thermal Diffusivity—Part 2: Transient Plane Heat Source (Hot Disc) Method. International Organization for Standardization: Geneva, Switzerland, 2022.
41. Górszczyk, J.; Malicki, K. Comparative Laboratory Tests of Thermal Conductivity of Road Materials using Two Measurement Methods. *Materials* **2025**, *18*, 1970. [CrossRef]
42. Demirtürk, D.; Ozturk, H.I.; Guler, M. A Comparative Analysis of the Thermal Conductivity Measurement of Asphalt Concrete under Steady-State and Transient Heat Transfer Conditions. *Mater. Struct.* **2026**, *59*, 91. [CrossRef]

Disclaimer/Publisher's Note: The statements, opinions and data contained in all publications are solely those of the individual author(s) and contributor(s) and not of MDPI and/or the editor(s). MDPI and/or the editor(s) disclaim responsibility for any injury to people or property resulting from any ideas, methods, instructions or products referred to in the content.